The H I angular momentum-mass relation

Kurapati, Sushma; Chengalur, Jayaram N.; Verheijen, Marc A. W.

IMPORTANT NOTE: You are advised to consult the publisher's version (publisher's PDF) if you wish to cite from it. Please check the document version below.

Document Version
Publisher's PDF, also known as Version of record

[Link to publication in University of Groningen/UMCG research database](#)

The H I angular momentum–mass relation

Sushma Kurapati [1,2]★ Jayaram N. Chengalur[1]★ and Marc A. W. Verheijen [1,3]★

[1]*National Centre for Radio Astrophysics, Tata Institute of Fundamental Research, P.O. Box 3, Pune 411007, India*
[2]*The Inter-University Centre for Astronomy and Astrophysics, Post Bag 4, Ganeshkhind, Pune, 411007, India*
[3]*Kapteyn Astronomical Institute, University of Groningen, P.O. Box 800, NL-9700 AV Groningen, the Netherlands*

ABSTRACT

We study the relationship between the H I specific angular momentum (j_g) and the H I mass (M_g) for a sample of galaxies with well-measured H I rotation curves. We find that the relation is well described by an unbroken power law $j_g \propto M_g^\alpha$ over the entire mass range (10^7–$10^{10.5}$ $M_\odot$), with $\alpha = 0.89 \pm 0.05$ (scatter 0.18 dex). This is in reasonable agreement with models which assume that evolutionary processes maintain H I discs in a marginally stable state. The slope we observe is also significantly different from both the $j \propto M^{2/3}$ relation expected for dark matter haloes from tidal torquing models and the observed slope of the specific angular momentum–mass relation for the stellar component of disc galaxies. Our sample includes two H I-bearing ultra-diffuse galaxies, and we find that their angular momentum follows the same relation as other galaxies. The only discrepant galaxies in our sample are early-type galaxies with large rotating H I discs, which are found to have significantly higher angular momentum than expected from the power-law relation. The H I discs of all these early-type galaxies are misaligned or counter-rotating with respect to the stellar discs, consistent with the gas being recently accreted. We speculate that late-stage wet mergers, as well as cold flows play a dominant role in determining the kinematics of the baryonic component of galaxies as suggested by recent numerical simulations.

Key words: galaxies: dwarf – galaxies: fundamental parameters – galaxies: kinematics and dynamics.

1 INTRODUCTION

Studies of the correlations between global parameters of galaxies (e.g. rotation velocity versus luminosity, or star formation rate versus stellar mass) provide critical observational tests of galaxy formation and evolution models. One specific parameter that is receiving increasing attention is the angular momentum. This is in part because it is only now that, thanks to large Integral Field Unit (IFU) surveys as well as large H I surveys, measurements of angular momentum are becoming available for a sizeable number of galaxies (e.g. Walter et al. 2008; Hunter et al. 2012; Sánchez et al. 2012; Bryant et al. 2015; Bundy et al. 2015; Stott et al. 2016). Further, our theoretical understanding of how galaxies acquire angular momentum is also rapidly evolving as numerical models become more sophisticated and better able to capture the details of the physics of the baryonic component of galaxies.

The traditional understanding was that galaxies acquire their angular momentum via tidal torquing of collapsing proto-haloes by neighbouring mass concentrations. In such models, the bulk of the angular momentum gain happens around the turn around time of the proto-halo and the angular momentum remains roughly constant after that epoch. The angular momentum of the final collapsed halo is generally quantified by its 'spin parameter' $\lambda_h = J_h|E_h|^{1/2}/(GM_h^{5/2})$ (where J_h is the total angular momentum of the halo, E_h the total energy, and M_h the total mass). Both analytical calculations (Peebles

1969) and numerical simulations (e.g. Bett et al. 2007; Rodríguez-Puebla et al. 2016) find that the spin parameter is roughly independent of the total mass of the halo. This leads to a scaling relation between the halo specific angular momentum j_h ($=J_h/M_h$) and the halo mass, viz. $j_h \propto M_h^{2/3}$. If one assumes that the baryonic matter and the dark matter have similar distributions at early times and that galaxies form by cooling and angular momentum conserving collapse of the baryonic component (Fall 1983; Mo, Mao & White 1998), then a similar scaling relation would be expected for the baryonic component of galaxies, viz. $j_{bar} \propto M_{bar}^{2/3}$. It has been found that such a scaling relation is indeed obtained for the stellar component of galaxies, although individual galaxies can deviate significantly from the relation and the constant of proportionality varies between early- and late-type galaxies, as well as with bulge fraction (Fall 1983; Romanowsky & Fall 2012; Fall & Romanowsky 2018).

This traditional understanding has been challenged by several numerical simulations (e.g. Desmond et al. 2017; Jiang et al. 2019) of galaxy formation that include the effects of mergers and cold flows. These simulations show that the collapsed baryonic component of galaxies does not arise solely from the cooling and contraction of the initial hot baryonic component of the proto-halo. Both mergers and 'cold' flows of baryonic material along filaments that penetrate deep into the halo (e.g. Kereš et al. 2005, 2009; Brooks et al. 2009) could result in a significant change in the final baryonic mass as well as the final angular momentum. The effect on the angular momentum depends on whether the merger was 'wet' (i.e. with a gaseous progenitor) or dry (i.e. with a gas-poor progenitor) as well as the relative orientation of the spin of the incoming material

★ E-mail: sushma@ncra.tifr.res.in (SK); chengalur@ncra.tifr.res.in (JNC); verheyen@astro.rug.nl (MAWV)

vis-a-vis that of the galaxy (see e.g. Naab et al. 2014; Choi & Yi 2017; Lagos et al. 2018). Additionally, the final baryonic mass as well as the angular momentum is affected by the energy input from stellar winds and supernovae, which could cause an outflow of material from the galaxy. The strength of the outflows depends on whether the supernovae explosions are clustered or not. Since clustering of supernovae typically happens only near the centres of galaxies (i.e. in regions where the material has low specific angular momentum), outflows lead to a preferential loss of low specific angular momentum material. This results in an increase in the specific angular momentum of the remaining material in the galaxy (Dutton 2009; Brook et al. 2011; Sharma, Steinmetz & Bland-Hawthorn 2012). As a consequence of these processes, the angular momentum of the galaxy is not determined during its formation phase but rather is affected by the entire evolutionary path of the galaxy. Both the morphology and the angular momentum appear to be driven more by evolutionary processes and a galaxy's merger history than the original spin parameter of the dark matter halo (see e.g. Stewart et al. 2017; Zjupa & Springel 2017; Jiang et al. 2019; Renzini 2020). For example, simulations show that accretion of low specific angular momentum or counter-rotating gas leads to a central compact galaxy ('blue nugget'), with an outer spheroidal stellar distribution, and possibly an outer counter-rotating disc, while accretion of co-rotating material typically leads to a disc-type galaxy with gas density stable against rapid gravitational collapse (see e.g. Zolotov et al. 2015; Jiang et al. 2019; Kretschmer, Agertz & Teyssier 2020).

Recent observational studies have also begun to indicate that the relationship between the specific angular momentum and the mass is more nuanced than a simple $j_{bar} \propto M_{bar}^{2/3}$ scaling. For the stellar j_s–M_s relation, Posti et al. (2018) and Posti et al. (2019) find an unbroken power law $j_s \propto M_s^\alpha$ with $\alpha \sim 0.55 \pm 0.02$ for all the galaxies in the stellar mass range of 10^7–$10^{11.5}$ M$_\odot$. On the other hand, for the gas j_g–M_g relation Mancera Piña et al. (2021) have recently reported a slope of 1.01 ± 0.04. Earlier studies have also found that gas-rich dwarf galaxies appear to have an excess baryonic specific angular momentum compared to that expected from the scaling relation for bulgeless spirals given by Obreschkow & Glazebrook (2014) (e.g. Butler, Obreschkow & Oh 2017; Chowdhury & Chengalur 2017; Kurapati et al. 2018). Kurapati et al. (2018) also find that the elevation in specific angular momentum occurs for the galaxies with masses lower than $\sim 10^9$ M$_\odot$. The scaling relation hence appears to depend both on the details of the galaxy morphology and which component (stars, gas) of the galaxy is under consideration.

Here, we study the relation between the baryonic specific angular momentum and mass and the H I specific angular momentum (j_g) and H I mass (M_g) for a diverse sample of gas-rich galaxies including H I-bearing ultra-diffuse galaxies (HUDs), normal dwarf galaxies, spiral galaxies, and early-type galaxies. We discuss the results in terms of the range of simulations discussed above. This paper is organized as follows. In Section 2.1, we describe the sample and observations. In Section 3, we determine the gas angular momentum and gas–mass relation. We present a discussion in Section 4 and summarize the main results in Section 5.

2 DETERMINATION OF SPECIFIC ANGULAR MOMENTUM

2.1 Sample

Our sample consists of a wide variety of galaxies including dwarf galaxies, HUDs, spiral galaxies, and early-type galaxies. For some galaxies, we present fresh measurements. We supplement this sample

with measurements that are available in the literature. We discuss first the galaxies for which we present fresh measurements.

The HUDs were selected from the 'more restrictive' sample of Leisman et al. (2017), with half-light radii $r_{g,eff} > 1.5$ kpc, $\mu_{g,0} > 24$ mag arcsec^{-2}, and g-band magnitude > -16.8 mag, i.e. more extreme stellar sizes as compared to their stellar magnitudes. We used new Giant Metrewave Radio Telescope (GMRT) observations to obtain H I morphologies and kinematics of two HUDs as part of a pilot study for a larger survey. We derive the rotation curves and H I surface brightness profiles for these galaxies using Fully Automated TiRiFiC (FAT; Kamphuis et al. 2015) by fitting a tilted ring model to the data cube. The derived rotation curves and surface brightness profiles for ultra-diffuse galaxies are shown in Figs A11 and A13, respectively.

Spiral galaxies are taken from the samples of Verheijen & Sancisi (2001). Verheijen & Sancisi (2001) presented results from a synthesis imaging survey of 43 galaxies in the nearby Ursa Major region using the Westerbork Synthesis Radio Telescope. We require a sample of galaxies where rotation curves can be reliably derived. Hence, we consider only the galaxies that are well resolved across the major axis and exclude the galaxies that are in interacting pairs or that have disturbed velocity fields. 16 of 43 galaxies remain after the imposition of these criteria. We use K-band luminosity profiles (as measured in Verheijen 2001) to calculate the stellar mass profiles since the uncertainties in the derivation of the mass-to-light ratio are much less in the mid-infrared compared to the optical. We assume a constant K-band mass-to-light ratio of 0.24 to calculate the stellar surface density profiles (Ponomareva et al. 2018). We use the rotation curves and the radial H I surface density profiles from Verheijen (2001) to calculate the baryonic and gas specific angular momentum.

The early-type galaxies were selected from the ATLAS^{3D} H I survey of a volume-limited, complete sample of 166 nearby early-type galaxies brighter than $M_K = -21.5$ (Serra et al. 2012). In constructing the sub-sample, we first restrict the selection to galaxies with morphologies later than $T > -4.0$. Serra et al. (2012) divided the galaxies with detected H I into four morphological classes, viz. (i) large discs – most of the H I rotates regularly and is distributed in a disc or a ring larger than the stellar body of the galaxy, (ii) small discs – most of the H I rotates regularly and is distributed in a small disc confined within the stellar body of the galaxy, (iii) unsettled – most of the H I exhibits an unsettled morphology (e.g. tails or stream of gas) and kinematics, and (iv) clouds – the H I is found in small, scattered clouds around the galaxy. In order to calculate the angular momentum accurately, we require a sample where reliable rotation curves can be derived. Hence, we have considered only the galaxies from the first class, i.e. those with large discs that have regular velocity fields. We derived the rotation curve for these galaxies using FAT or ^{3D}Barolo (Di Teodoro & Fraternali 2015) on the final ATLAS^{3D} data products, i.e H I cubes with a typical angular resolution of ~ 35 arcsecs. We chose the galaxies that are well resolved across its major axis (>6 beams). Our final sample consists of those galaxies for which reliable rotation curves could be obtained by FAT or BAROLO. BAROLO was used to derive the rotation curve for only one of the galaxies (NGC 3941), since the FAT-derived rotation curve was unreliable. Two of the early-type galaxies (NGC 3626 and NGC 3941) have companions, which were excluded for the measurements of mass and specific angular momentum. The derived rotation curves and surface brightness profiles for the final sample of early-type galaxies are shown in Figs A12 and A14, respectively. In Figs A1–A10, we show (i) the integrated H I intensity map contours overlaid on the optical image, and (ii) Position-velocity (PV) diagram taken along the major axis of the galaxy with the rotation curves overlaid on them.

The dashed lines indicate the systemic velocity and kinematic centre. The overplotted violet triangles represent the rotation curve derived by 'FAT' (iii) the intensity-weighted first moment of the galaxy, and (iv) velocity field of the best-fitting FAT model for all the HUDs and early-type galaxies. We find that all the rotation curves broadly follow the PV diagram. We note that PV diagrams are not fully representative of the rotation curve as they may reflect the effects of non-circular motion while FAT and other algorithms also take pixels off the kinematic major axis into account.

As mentioned above, in our analysis we also use the published data from various earlier studies; the details are given in the relevant sections.

2.2 Measuring mass and specific angular momentum

The H I mass was calculated using the standard formula, $M_{HI} = 2.36 \times 10^5 D^2 \int S \, dv \, M_\odot$, where D is the distance in Mpc, S is the flux density in Jy, and dv is in km s^{-1} (Roberts 1962). The distances for early-type galaxies are taken from Cappellari et al. (2011), which were obtained with the surface brightness fluctuation method. These distance estimates have an error of ~7–10 per cent. The distance estimates for the ultra-diffuse dwarf galaxies (UDGs) are taken from Leisman et al. (2017), which were calculated using the ALFALFA flow model, and the distance uncertainties due to proper motions are ≲15 per cent. The distances for the Ursa Major spiral galaxies are taken from Sorce et al. (2014), which were derived by using the Tully Fisher relation as an empirical distance estimator, which provides a distance accuracy of ~3–10 per cent. We assume a conservative error of 15 per cent on distance measurements for all the galaxies. The quoted uncertainties on gas mass are based on the errors on the distance measurements as well as the error on flux densities. The error on the flux density is dominated by the calibration uncertainties, which are typically ~10 per cent. We do not consider the mass-to-light ratio uncertainties while calculating the uncertainties of baryonic masses for the ultra-diffuse galaxies as they are dominated by the gas mass. We calculate the uncertainties of the baryonic masses for the UMa spirals (following Lelli, McGaugh & Schombert 2016) by

$$\delta_{M_{bar}} = \sqrt{\delta_{M_g}^2 + (\gamma_* \delta_{L_*})^2 + (L \delta_{\gamma_*})^2 + \left(2 M_{bar} \frac{\delta_D}{D}\right)^2}, \quad (1)$$

where δ_g and δ_L are the errors on M_g and L due to uncertainties on total fluxes and δ_γ is the uncertainty in mass-to-light ratio. We assume $\delta_{\gamma_*} \sim 0.1$ dex for K-band data (Ponomareva et al. 2018). The specific angular momentum j is computed by numerically evaluating the integral,

$$j \equiv \frac{J}{M} = \frac{\int_0^R dr 2\pi r^2 \Sigma(r) v(r) cos[\delta i(r)]}{\int_0^R dr 2\pi r \Sigma(r)}, \quad (2)$$

where $\Sigma(r)$ is the azimuthally averaged surface density, $v(r)$ is the circular velocity at radius r, $\delta i(r)$ is the difference in inclination with respect to the central disc inclination, and R is the radius of the gas disc. This integral is evaluated separately for the stellar, the gaseous, and the baryonic components of the galaxy. The procedure used for the estimation of specific angular momentum is similar for the galaxies from this work and for the galaxies that are taken from the literature. In this work, only the stellar, H I, and helium contributions to the baryonic mass are considered. Hence, the total baryonic surface density is $\Sigma_b = \Sigma_* + 1.35 \Sigma_{HI}$, where the 1.35 factor accounts for the H e contribution. No correction was made for molecular hydrogen as well as ionized gas. The optical deprojected

radial surface brightness profiles were derived by fitting elliptical annuli to the optical images by using the ELLINT task in the GIPSY package. The specific angular momentum of gas, stars, and baryons was computed by numerically evaluating the integral in equation (1). For all quantities, the integral converges within the error bars. The uncertainties on the specific angular momentum of the various components are based on the errors on distance measurements, on rotation velocities, surface brightness values, and inclination values. The uncertainty in j_k (k being stars or gas) is given by:

$$\frac{\delta_{j_k}}{j_k}$$

$$= \sqrt{\left(\frac{\delta_D}{D}\right)^2 + \left(\frac{\delta_i}{\tan(i)}\right)^2 + \sum_i^N \left(\frac{\delta_{v_i}}{v_i} \cdot \frac{J_i}{J}\right)^2 + \sum_i^N \left(\frac{\delta_{S_i}}{S_i} \cdot \frac{J_i}{J}\right)^2}$$

$$(3)$$

where i is the inclination (δ_i is its uncertainty). v_i is the rotation velocity at each point on rotation curve (δ_{v_i} is its uncertainty), S_i is the surface brightness value at each point on surface brightness profile (δ_{S_i} is its uncertainty), J_i is the evaluated angular momentum in each ring, and J is the total angular momentum of galaxy. The errors on specific angular momentum are often dominated by the errors on distance measurement.

In Tables A1 and A2, we present the measurements of stellar, gas, and baryonic mass and specific angular momentum of UMa spiral galaxies and ultra-diffuse galaxies, respectively: The columns are as follows. Column (1) name of the galaxy; (2) stellar mass; (3) gas mass; (4) total baryonic mass; (5) stellar specific angular momentum; (6) gas specific angular momentum; and (7) baryonic specific angular momentum. In Table A3, we show the properties and the measurements of the gas mass and gas specific angular momentum of the early-type galaxies. The columns are as follows. (1) name of the galaxy; (2) morphology; (3) distance in Mpc; (4) gas mass; (5) gas specific angular momentum; and (6) notes on galaxies.

2.3 Convergence criteria

We show the cumulative specific angular momentum profiles for two HUDs (both j_{bar} and j_g profiles), 16 UMa spirals (both j_{bar} and j_g profiles), and eight early-type galaxies (only j_g profiles) in Figs A15–A17, respectively. We normalize the specific angular momentum and radius axes to allow the comparison between the profiles. We also make a quantitative assessment of the convergence of these profiles. We follow Posti et al. (2018) to determine whether the specific angular momentum of a galaxy has converged or not. We select galaxies satisfying the following criteria:

$$\frac{j(<R_N) - j(R_{N-1})}{j(R_N)} < 0.1 \quad \&\& \quad \frac{d \log(j(<R))}{d \log(R)}\bigg|_{R_N} < 0.5 \quad (4)$$

i.e. that the last two points of the j profile differ by less than 10 per cent and that the logarithmic slope of the j profile in the outermost point is less than 1/2. We find that all the galaxies except two early-type galaxies (NGC 3626 and NGC 6798) follow the convergence criterion.

We also fit a function $\mathcal{P} = k \cdot \exp(-a/x)$ (which is zero at x→ 0^+ becomes constant as $x \to \infty$) to the last three points of the cumulative j profile. We then take the ratio r_k (k being baryons/gas) of j_k at last measured point to the maximum value that $\mathcal{P}$ would have if extrapolated to infinity. This ratio (i.e. the convergence factor) is calculated for all the j_{bar} and j_{gas} profiles and listed for all the galaxies in Tables A4–A6. Only two of the early-type galaxies (NGC 3626 and

NGC 6798) and one of the ultra-diffuse galaxies have a convergence factor of <0.7.

Several angular momentum studies, e.g. Murugeshan et al. (2020) and Elson (2017), do not check for convergence. Disc galaxies show a range of rotation curve shapes with low-mass galaxies typically having rising rotation curves. However, in general, dwarf galaxies show a large diversity of rotation curve shapes, even at fixed maximum rotation speed (e.g. Oman et al. 2015). Restricting the analysis to a set of galaxies that meet a user-defined convergence criterion may lead to a non-representative sample, particularly for the galaxies with lower baryonic masses. For studies where one is considering the specific angular momentum of the galaxy disc (as opposed to making inferences about the halo), it is not clear that a restriction of the sample to those whose specific angular momentum curves meet a user-defined convergence is essential.

3 RESULTS

3.1 Specific angular momentum of the H I disc

As discussed in the introduction, recent simulations indicate that the angular momentum of galaxies is governed more by evolutionary processes and the physics of the baryonic material than by the initial spin of the 'parent' dark matter halo. Numerical simulations also support the picture that star formation occurs in marginally stable gas discs, where inflows provide both the gas required for the star formation and the energy to keep the discs marginally stable against gravitational instability (e.g. Dekel et al. 2013). Models of disc galaxies where the discs are critically stable also appear to provide a reasonable description of the specific angular momentum–mass relation of the gas discs of local galaxies (e.g. Zasov 1974; Zasov & Zaitseva 2017; Kurapati et al. 2018; Romeo 2020). Observational constraints on models where the gas mass and angular momentum of H I discs are set by the requirement that the disc be critically stable have been presented by, e.g. Obreschkow et al. (2016) and Zasov & Zaitseva (2017). It would hence be interesting to look at how well such models fit the H I specific angular momentum (j_g) and the H I mass (M_g) for our heterogeneous sample of galaxies.

We show in Fig. 1 the H I-specfic angular momentum and H I gas mass relation for our sample galaxies along with other samples taken from the literature (details are given in the figure caption). Interestingly, the galaxies show a smooth j_g–M_g relation across the entire mass range. We estimate the best-fitting linear regression between j_g and M_g by using the BCES algorithm (Akritas & Bershady 1996) that accounts for errors on both j_g and M_g as well as for the fact that these errors are correlated. The best-fitting j_g–M_g relation is given by $j_g = qM_g^\alpha$ with $\alpha = 0.89 \pm 0.05$ and $\log_{10} q = -5.42 \pm 0.41$. We do not include early-type galaxies while fitting for the j_g–M_g relation since these galaxies are peculiar in that the gas is counter-rotating or misaligned with the stellar kinematics. We discuss these galaxies further below. The existence of such a relation between the H I mass and the H I specific angular momentum (suggested earlier also by e.g. Zasov 1974) is interesting in itself, and we return to this in Section 4. We also note that the slope that we find for the j_g–M_g relation is significantly different from that seen for the j_s–M_s relation (i.e. 0.55 ± 0.02) by Posti et al. (2019). The slope we get is slightly smaller than (but statistically consistent with) the value of 1.02 ± 0.04 recently reported by Mancera Piña et al. (2021). We return to a discussion of this in Section 4. Here, we focus on how the relation that we find compares with expectations from the critically stable disc model.
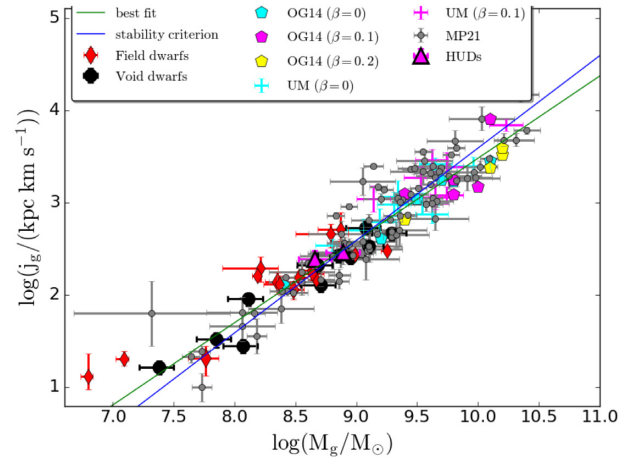

Figure 1. Log j_g–log M_g of 2 HUDs (magenta triangles) from this work, 11 dwarfs residing in Lynx–Cancer void (black circles) from Kurapati et al. (2018), 17 field dwarfs (red diamonds from Butler et al. (2017) and Chowdhury & Chengalur (2017), 16 spirals residing in the UMa cluster (plus symbols) from this work, 15 spirals from Obreschkow & Glazebrook (2014) (pentagons), and 84 galaxies from Mancera Piña et al. (2021) (grey circles). The cyan, magenta, and yellow symbols (plus symbols and pentagons) indicate spiral galaxies with bulge fractions, $\beta = 0$, $\beta = 0.1$, and $\beta = 0.2$, respectively. The green line indicates the best fit for the j_g–M_g relation using the linear regression. The blue line represents the stability criterion [j_{HI} x 11 km s^{-1}/(G M$_{HI}$) $\sim$ 1] from Romeo (2020).

The commonly used criterion for stability is the Toomre Q parameter. Strictly speaking, the Toomre criterion is for a thin single-component disc, while at least some of the galaxies that we are analyzing have significant stellar masses as well as a non-negligible disc thickness. Issues associated with applying the Toomre-Q criterion to such galaxies have been discussed in detail in Zasov & Zaitseva (2017) and Romeo (2020). Romeo (2020), in particular, takes a phenomenological approach and suggests that the different components (molecular, atomic, stellar) of galaxy discs follow scaling laws derived from the relation

$$\frac{j_i \hat{\sigma}_i}{G M_i} \approx 1,$$

where $\hat{\sigma}_i = \bar{\sigma}_i / A_i$, with $\bar{\sigma}_i$ being the disc averaged velocity dispersion of component i (H I, H$_2$, or stars), and A_i is the mass-averaged Toomre-Q parameter. The value of $\hat{\sigma}_i$ is not derived from fundamental principles but is instead determined by a fit to observational data. Romeo (2020) uses data from Leroy et al. (2008) (which overlaps with the Obreschkow & Glazebrook 2014 sample) to determine the value for $\hat{\sigma}_i$. For the H I component, the derived value is 11 km/s. We show this empirical relation, $\log(j) = \log(M)$-6.41 (with $\hat{\sigma}_i = 11$ km/s) in Fig. 1. As can be seen, it provides a good fit to the data, the majority of which is independent from the sample used by Romeo (2020). This further supports the idea that the structure of the H I discs in galaxies settles to a critical density, as would happen in models where the star formation rate (and hence mass outflow rate) is driven by the mass inflow rate.

As discussed in the introduction, simulations also show that spheroidal stellar distributions with extended counter-rotating gas discs could arise in systems where there has been a recent accretion of gas whose spin is not aligned with that of the parent galaxy (e.g. Kretschmer et al. 2020). In the context of such models, it would be interesting to examine the position of extremely gas-rich early-type galaxies in the $j_g - M_g$ plane. As can be seen from
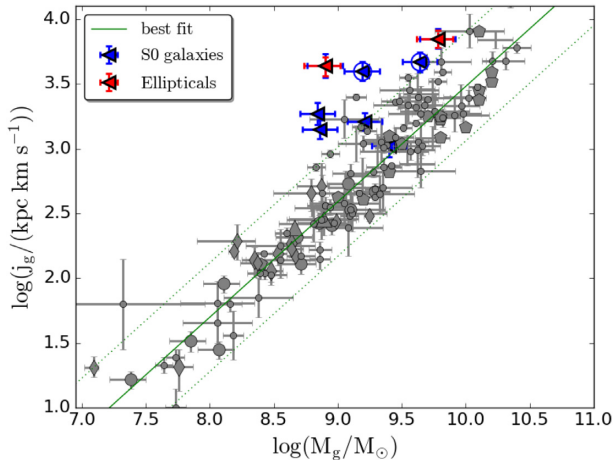
Figure 2. The location of early-type galaxies with large regular H I discs (blue open triangles) and the other galaxies (symbols are the same as in Fig. 1) in the j_g–M_g plane. The green solid line indicates the best-fitting line using the linear regression for all the galaxies except early-type galaxies. The green dotted lines indicate 3σ scatter around the relation. The early-type galaxies that do not follow the convergence criterion are marked with a circle around the blue open triangles. The H I discs in gas-rich early-type galaxies have high specific angular momentum compared to other galaxies with similar H I mass.

Table A3 in appendix, for many of the galaxies in our sample the gas is counter-rotating or misaligned with the stellar kinematics, consistent with results from simulations. Fig. 2 shows the location of early-type galaxies, as well as all our other sample galaxies in the j_g–M_g plane. The green solid line indicates the best-fitting line using the linear regression for all the galaxies except the early-type galaxies, and green-dotted lines indicate 3σ vertical scatter. As can be seen, most of the early-type galaxies lie above the 3σ scatter, i.e. their H I discs have significantly higher specific angular momentum as compared to other galaxies with the same H I mass. A Kolmogorov–Smirnov test (Fasano & Franceschini 1987, https://github.com/syrte/ndtest/blob/master/ndtest.py) gives a probability of 7×10^{-4} for the early-type galaxies being drawn from the same distribution as the other galaxies.

Two of these early-type galaxies (NGC 3626 and NGC 6798, marked with a circle around the blue open triangles in Fig. 2) do not satisfy the convergence criterion. We note that they do not appear to have discrepant j_g as that of the early-type galaxies with converged specific angular momentum curves. If the lack of convergence means that these two galaxies have a higher specific angular momentum than measured, it does not affect the result that the early-type galaxies in our sample have significantly higher j_g than expected from the j_g–M_g power law. Our observations hence support the picture in which these gas-rich early-type galaxies have acquired the gas via a recent inflow of high but misaligned specific angular momentum gas. The elevated specific angular momentum is consistent with the decreased star formation efficiency of early-type galaxies since higher angular momentum stabilizes the gas against Jeans instabilities and subsequent star formation (Toomre 1964; Obreschkow et al. 2016).

We also show the scaling relation between the atomic gas fraction (f_{atm}) and the stability parameter (q) for all the galaxies in our sample in Fig. 3 for which these parameters are available. The dotted line shows the relation expected from Obreschkow et al. (2016). We find that all the galaxies in our sample largely follow the relation consistently. We do not show early-type galaxies in this figure since
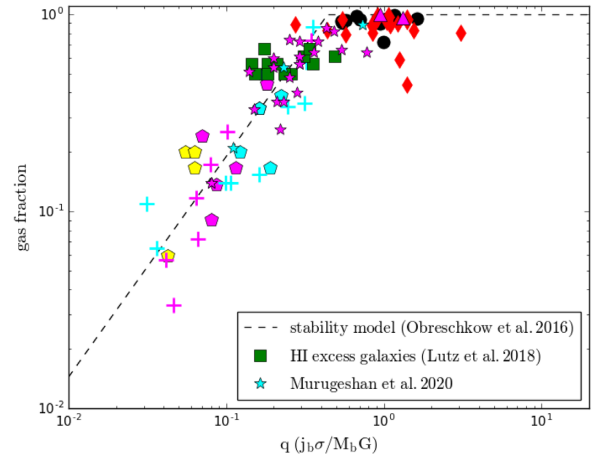

Figure 3. The atomic gas mass to baryonic mass fraction versus the global stability parameter q for all the galaxies in our sample (symbols are the same as in Fig. 1). We also show galaxies from Murugeshan et al. (2020) [cyan stars ($\beta = 0$) and magenta stars ($\beta = 0.1$)] and the H I excess galaxies from Lutz et al. (2018) (green squares). These galaxies were not included in the earlier plots for the j_g–M_g relation because j_g is not available for these galaxies. We do not show the galaxies from Mancera Piña et al. (2021) as q values were not presented. The dotted line is the relation predicted by Obreschkow et al. (2016).

we cannot measure their baryonic specific angular momentum as the gas does not in general co-rotate with the stars for these galaxies. The dwarf galaxies lie in the saturated region ($f_{atm} \sim 1$). We also show the H I excess (higher atomic gas fraction) galaxies from Lutz et al. (2018) for comparison; they follow the relation between the atomic to baryonic mass fraction and the global stability parameter given by Obreschkow et al. (2016).

3.2 Baryonic specific angular momentum

Several earlier studies (e.g. Obreschkow & Glazebrook 2014; Kurapati et al. 2018; Murugeshan et al. 2020; Mancera Piña et al. 2021) have studied the correlation between the specific angular momentum and mass of the baryonic (i.e. gas + stars) component of galaxies. In particular, Kurapati et al. (2018) investigated the relation considering the baryonic mass for a sample of gas-rich dwarf galaxies in a range of environments, using the bulgeless spiral relation found by Obreschkow & Glazebrook (2014) for comparison. They concluded that the baryonic specific angular momentum of dwarfs was higher as compared to the extrapolation of the trend seen for higher mass bulgeless spirals. The increase in specific angular momentum was found to set in at a mass threshold of $\sim 10^9\, M_\odot$. However, more recent studies (e.g. Mancera Piña et al. 2021) find that the j_{bar}–M_{bar} relation is well fit by a single power law.

Fig. 4 shows the relation between the baryonic specific angular momentum and the baryonic mass for the UMa sample of spiral galaxies from this work, along with the galaxies in Obreschkow & Glazebrook (2014), Butler et al. (2017), Chowdhury & Chengalur (2017), Elson (2017), Kurapati et al. (2018), Murugeshan et al. (2020), and Mancera Piña et al. (2021) We do not use the early-type galaxies from the current work in this analysis since, as discussed above, the gas does not in general co-rotate with the stars. If fit a single power law to our sample (red dashed line in Fig. 4), we obtain a slope 0.55 ± 0.02 in good agreement with the slope measured by Mancera Piña et al. (2021). However, all the galaxies having $M_{bar} \lesssim 10^8\, M_\odot$ lie significantly below the relation while the galaxies having
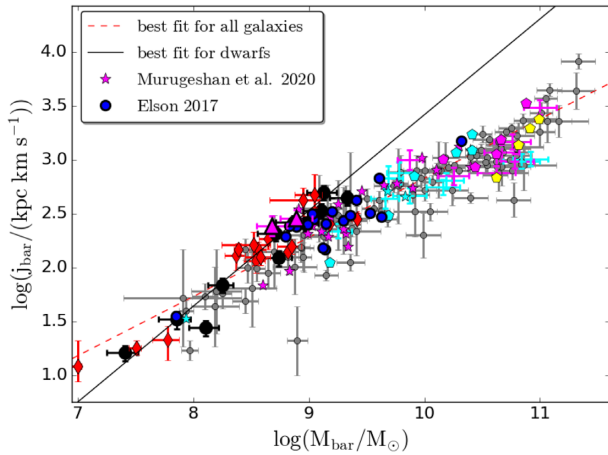
Figure 4. The log j_{bar}–log M_{bar} plane. The black solid line is the best-fitting line for the dwarf galaxies from Kurapati et al. (2018) and the red dashed line is the best-fitting line for all the galaxies. The symbols are the same as in Fig. 1. The blue circles represent galaxies (only the galaxies with reliable rotation curves) from Elson (2017).

10^8 $M_\odot \lesssim M_{bar} \lesssim 10^9$ $M_\odot$ are consistently above the relation. In this context, we note that the Mancera Piña et al. (2021) sample does not contain galaxies with baryonic mass lower than $10^8 M_\odot$. This suggests that there may be some curvature in the j_{bar}–M_{bar} relation, and it may not be best described by a single unbroken power law.

In order to test how well the j_{bar}–M_{bar} relation is described, a single unbroken power law, we estimate the best-fitting linear regression between j_{bar} and M_{bar} independently for two separate mass ranges, viz. galaxies with $M_{bar} > 10^9$ $M_\odot$ and for the galaxies with $M_{bar} < 10^9$ $M_\odot$. We find significantly different slopes for the j_{bar}–M_{bar} relation, with a slope of 0.80 ± 0.05 for low-mass galaxies and a slope of 0.52 ± 0.02 for high-mass galaxies. This suggests that a single power law is not the best description of the data. On the other hand, the slopes of j_g–M_g relation match within the error bars for low-mass galaxies ($\sim 0.85 \pm 0.05$) and high-mass galaxies ($\sim 0.93 \pm 0.07$), suggesting that a single power law is an adequate description.

We also use the 'Chow test' (Chow 1960) to test whether the j_{bar}–M_{bar} relation is well fit by a single unbroken power law. The test checks for the statistical significance of postulated change in slope in a regression. We run the Chow test on both the j_{bar}–M_{bar} and the j_g–M_g relations (https://github.com/jtloong/chow_test) to test the significance of a difference in slope between the high- and low-mass ends, with the nominal dividing point taken as 10^9 $M_\odot$. As per the Chow test, the null hypothesis that the baryonic j–M relation follows an unbroken power law is rejected at a high significance, with a p value of 5.5×10^{-5}. This indicates that there is a significant change in slope, with a broken power law providing a better fit. We note that the test does not independently identify a sharp break point; a curved relation with a gradual change in slope as one moves from lower to higher baryonic masses would also be better fit by a broken power law rather than a single one. In contrast to this, we find a fairly large p value (0.2) for the gas j–M relation, which indicates that it is adequately fit by a single power law. We note that the number of galaxies with low baryonic masses in the sample is still quite modest, and it is important to increase the sample size at the low mass end. We return to a discussion of the possible reasons for the change in slope seen in the $j_{bar} - M_{bar}$ relation in the next section.

Finally, we draw attention to one more feature in Fig. 4, the location of the ultra-diffuse dwarfs. Ultra-diffuse dwarf galaxies are a recently discovered population of very low-surface brightness galaxies, which have stellar masses of dwarfs but have sizes as large as L_* galaxies (van Dokkum et al. 2015). The majority of the UDGs are red and appear more common in clusters. However, galaxies with extreme ratios of stellar mass to stellar scale length were also discovered in H I surveys of isolated environments (e.g. Leisman et al. 2017). These galaxies are called H I-bearing ultra-diffuse galaxies, which are bluer and have significant reservoirs of H I as compared to the UDGs in the clusters. Several formation scenarios have been proposed to explain the formation of the UDGs. Some authors propose a scenario in which UDGs are failed Milky Way-like galaxies that lost their gas after forming the first stars (van Dokkum et al. 2015), and others argue that they are genuinely dwarf galaxies residing in high spin parameter haloes (Amorisco & Loeb 2016). These formation scenarios can be tested by measuring the angular momentum of UDGs and comparing them to the normal dwarf galaxies. Fig. 4 shows the baryonic specific angular momentum versus the baryonic mass of H I-bearing UDGs (magenta triangles) and normal dwarf galaxies of similar masses. We find that the specific angular momentum of H I-bearing UDGs is similar to other normal dwarf galaxies at a given mass. This is in contrast with the formation scenarios that predict that UDGs are genuinely dwarf galaxies residing in high spin haloes. We note that our result is in contradiction with a recent analysis by Mancera Piña et al. (2020), who find that ultra-diffuse galaxies have higher-than-average *stellar* specific angular momentum but have circular velocities much lower than galaxies with similar baryonic mass. They assume flat rotation curves and exponential light curves and approximately the stellar specific angular momentum to be the product of circular velocity and the stellar disc scale length since they lack the resolution to integrate angular momentum over the entire disc. This, along with the very small size of our sample, makes it important to confirm these results with high-resolution observations of a larger sample.

4 DISCUSSION

As we saw above, both the j_g–M_g relation (this work and Mancera Piña et al. 2021) and the j_s–M_s relation (Posti et al. 2018) follow an unbroken power law over the mass range of 10^7–$10^{10.5}$ $M_\odot$. However, their slopes are very different, viz. with slopes of 0.89 ± 0.05 (this work) and 0.55 ± 0.02 (Posti et al. 2018), respectively. In contrast to these relations, the j_{bar}–M_{bar} relation is better fit by a broken power law, with gas-rich low-mass galaxies having higher specific angular momentum compared to the extrapolated trend from high-mass galaxies. We test the scenario that this increase in baryonic specific angular momentum essentially reflects the different relative contributions of the stellar and gas angular momenta to the total baryonic angular momentum following from the different slopes of stellar and gas j–M relations.

We calculate the general expected trend of j_{bar} with M_{bar} by using the observed M_g–M_s and j_g–M_g and j_s–M_s relations as well as the relation between M_{HI} and M_s from Maddox et al. (2015). The predicted j_{bar}–M_{bar} curve from these relations is shown in Fig. 5, where we have included the contribution of helium to the gas mass by multiplying M_{HI} by a factor of 1.35. For the predicted relation, we have used the median H I mass values and their 1σ uncertainties derived for galaxies in the Maddox et al. (2015) sample for which SDSS spectra are available. The blue solid curve indicates the expected j_{bar}–M_{bar} relation and the blue-shaded region indicates the 1σ scatter. In addition, the relation obtained if we use the relation
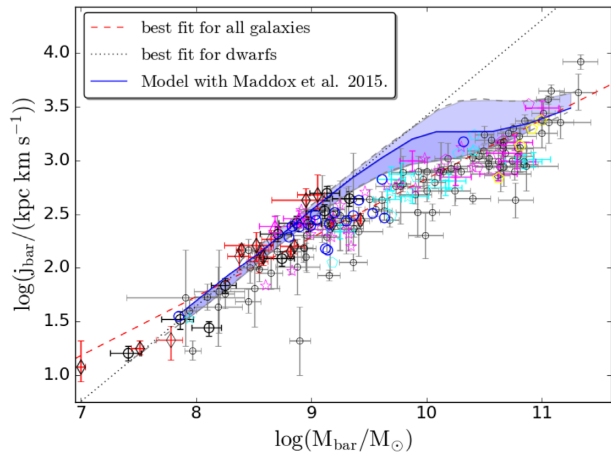
Figure 5. The log j_{bar}–log M_{bar} plane. The black dotted line is the best-fitting line for the dwarf galaxies from Kurapati et al. (2018) and the red dashed line is the best-fitting line for all the galaxies. The symbols are the same as in previous figure. The model is shown as blue-shaded region.

from Maddox et al. (2015) derived from the sample that includes galaxies without SDSS spectrum matches the blue curve within the 1σ scatter. As can be seen, the model curve is in broad qualitative agreement with the data showing a change in slope around $10^9 M_\odot$, although the j_{bar} values in this mass range are somewhat larger than the observed points. We note that the actual gas fractions of the sample being used would shift the location of the points in the j_{bar}–M_{bar} plane. However, the broad qualitative agreement between this simple model and the data supports the idea that the different slopes obtained at the low- and high-mass ends of the $j_{bar} - M_{bar}$ relation are a consequence of the changing contribution of the stars and gas to the total angular momentum at the high and low M_{bar} ends.

It is also interesting to ask how the power-law relations between the specific angular momentum and the mass fit in with the other known scaling relations? To address this question, we consider a simple model galaxy where the stars and gas have exponential surface brightness profiles with scale lengths r_s and r_g as well as a flat rotation curve with $V(r) = V_c$. This gives $j \propto V_c r$. From this expression, we calculate the expected slope (α_s) for the j_s–M_s relation by using the stellar mass size relation, $r_s \propto M_s^{0.28}$ (Bell & de Jong 2001) and the stellar TF relation, $V_c \propto M_s^{0.31}$ (Bloom et al. 2017), which gives $\alpha_s \sim 0.28 + 0.31 = 0.59$, which compares well with the observed slope of $\sim 0.55 \pm 0.02$. For the gas-rich galaxies, we use the baryonic TF relation, $V_c \propto M_{bar}^{0.33}$ (Ponomareva et al. 2018) and assume that the baryons are dominated by gas for the dwarf galaxies, which gives $V_c \propto M_g^{0.33}$. Observations suggest that the H I mass and radius are related as $r_g \propto M_g^{0.51}$ (Wang et al. 2016). This also arises from simulations if we assume an exponential H I disc, with the inner radius and outer radius being set by molecular transition and observational threshold for detecting H I (Obreschkow et al. 2009). The combination of baryonic TF relation and the gas mass-size relation gives the slope (α_g) for the j_g–M_g relation, $\alpha_g \sim 0.51 + 0.33 = 0.84$, in excellent agreement with what we observe. For less gas-rich galaxies, if we combine the stellar TF relation $V_c \propto M_s^{0.31}$ from Bloom et al. (2017) and the gas fraction relation $M_g/M_s = M_s^{-0.53}$ from Romeo (2020), we find $V_c \propto M_g^{0.66}$ and $\alpha_g \sim 0.66 + 0.51 = 1.17$ in reasonable agreement with what we observe. We cannot determine the predicted values of the intercepts, since they depend on the ratio of the size of the HI disc to its scale length, which is not well measured.

5 SUMMARY AND CONCLUSIONS

We have examined the relation between the H I mass and the H I specific angular momentum for a sample of galaxies with well-measured rotation curves that spans a range of morphology. Combining this with data from the literature, we find that the relation is well fit by an unbroken power law over the mass range of 10^7–$10^{10.5}$ $M_\odot$. The scatter in this relation is small, and this supports earlier suggestions that the relationship between the angular momentum and the mass is a fundamental scaling relation for galaxies. The slope that we measure for the power-law 0.89 ± 0.05 is also significantly different from that expected for dark matter haloes from tidal torquing models that predict $j \propto M^{2/3}$, as well as the observed slope of 0.55 ± 0.02 for the stellar component of disc galaxies. The slope we get for the $j_g - M_g$ relation is slightly smaller than (but statistically consistent with) the value of 1.02 ± 0.04 recently reported by Mancera Piña et al. (2021). Our sample includes two HUDs, and we find that they lie along the relationship defined by the other galaxies in our sample. The only discrepant galaxies are early-type galaxies with large well-rotating discs. These are found to have excess angular momentum compared to that predicted by the relation. In all of these galaxies, the H I disc also appears to be kinematically distinct from the stellar disc, indicating that it represents recently acquired material. Overall, our observation leads us to suggest that the kinematics of the baryonic component of gas-rich galaxies is more affected by cold flows and late-stage mergers than by the spin parameter of the 'parent' dark matter halo as suggested by recent numerical simulations. We also find that the $j_{bar} - M_{bar}$ relation is better fit by a broken power law than a single power law, indicating that there is some curvature in this relation. We suggest that the change in slope of the $j_{bar} - M_{bar}$ relation arises from the changing gas-to-stellar mass ratio with mass as well as the different slopes of the $j_s - M_s$ and $j_g - M_g$ relations.

DATA AVAILABILITY

The data presented for H I-bearing ultra-diffuse galaxies are available on the GMRT archive at: https://naps.ncra.tifr.res.in/goa/ and can be accessed with proposal id 34_091. The final ATLAS[3D] data products, i.e. H I data cubes of early-type galaxies, are available on NASA/IPAC Extragalactic Database (https://ned.ipac.caltech.edu/).

REFERENCES

Akritas M. G., Bershady M. A., 1996, ApJ, 470, 706
Amorisco N. C., Loeb A., 2016, MNRAS, 459, L51
Bell E. F., de Jong R. S., 2001, ApJ, 550, 212

Bett P., Eke V., Frenk C. S., Jenkins A., Helly J., Navarro J., 2007, MNRAS, 376, 215

Bloom J. V. et al., 2017, MNRAS, 472, 1809

Brook C. B. et al., 2011, MNRAS, 415, 1051

Brooks A. M., Governato F., Quinn T., Brook C. B., Wadsley J., 2009, ApJ, 694, 396

Bryant J. J. et al., 2015, MNRAS, 447, 2857

Bundy K. et al., 2015, ApJ, 798, 7

Butler K. M., Obreschkow D., Oh S.-H., 2017, ApJ, 834, L4

Cappellari M. et al., 2011, MNRAS, 413, 813

Choi H., Yi S. K., 2017, ApJ, 837, 68

Chow G. C., 1960, Econometrica, 28, 591

Chowdhury A., Chengalur J. N., 2017, MNRAS, 467, 3856

Dekel A., Zolotov A., Tweed D., Cacciato M., Ceverino D., Primack J. R., 2013, MNRAS, 435, 999

Desmond H., Mao Y.-Y., Wechsler R. H., Crain R. A., Schaye J., 2017, MNRAS, 471, L11

Di Teodoro E. M., Fraternali F., 2015, MNRAS, 451, 3021

Dutton A. A., 2009, MNRAS, 396, 121

Elson E. C., 2017, MNRAS, 472, 4551

Fall S. M., 1983, in Athanassoula E., ed., Proc. IAU Symp. 100, Internal Kinematics and Dynamics of Galaxies. D. Reidel Publishing Co, Dordrecht, p. 391

Fall S. M., Romanowsky A. J., 2018, ApJ, 868, 133

Fasano G., Franceschini A., 1987, MNRAS, 225, 155

Hunter D. A. et al., 2012, AJ, 144, 134

Jiang F. et al., 2019, MNRAS, 488, 4801

Kamphuis P., Józsa G. I. G., Oh S.-. H., Spekkens K., Urbancic N., Serra P., Koribalski B. S., Dettmar R.-J., 2015, MNRAS, 452, 3139

Kereš D., Katz N., Weinberg D. H., Davé R., 2005, MNRAS, 363, 2

Kereš D., Katz N., Fardal M., Davé R., Weinberg D. H., 2009, MNRAS, 395, 160

Kretschmer M., Agertz O., Teyssier R., 2020, MNRAS, 497, 4346

Kurapati S., Chengalur J. N., Pustilnik S., Kamphuis P., 2018, MNRAS, 479, 228

Lagos C. d. P., Schaye J., Bahé Y., Van de Sande J., Kay S. T., Barnes D., Davis T. A., Dalla Vecchia C., 2018, MNRAS, 476, 4327

Leisman L. et al., 2017, ApJ, 842, 133

Lelli F., McGaugh S. S., Schombert J. M., 2016, ApJ, 816, L14

Leroy A. K., Walter F., Brinks E., Bigiel F., de Blok W. J. G., Madore B., Thornley M. D., 2008, AJ, 136, 2782

Lutz K. A. et al., 2018, MNRAS, 476, 3744

Maddox N., Hess K. M., Obreschkow D., Jarvis M. J., Blyth S. L., 2015, MNRAS, 447, 1610

Mancera Piña P. E. et al., 2020, MNRAS, 495, 3636

Mancera Piña P. E., Posti L., Fraternali F., Adams E. A. K., Oosterloo T., 2021, A&A, 647, A76

Mo H. J., Mao S., White S. D. M., 1998, MNRAS, 295, 319

Murugeshan C., Kilborn V., Jarrett T., Wong O. I., Obreschkow D., Glazebrook K., Cluver M. E., Fluke C. J., 2020, MNRAS, 496, 2516

Naab T. et al., 2014, MNRAS, 444, 3357

Obreschkow D., Glazebrook K., 2014, ApJ, 784, 26

Obreschkow D., Croton D., De Lucia G., Khochfar S., Rawlings S., 2009, ApJ, 698, 1467

Obreschkow D., Glazebrook K., Kilborn V., Lutz K., 2016, ApJ, 824, L26

Oman K. A. et al., 2015, MNRAS, 452, 3650

Peebles P. J. E., 1969, ApJ, 155, 393

Ponomareva A. A., Verheijen M. A. W., Papastergis E., Bosma A., Peletier R. F., 2018, MNRAS, 474, 4366

Posti L., Fraternali F., Di Teodoro E. M., Pezzulli G., 2018, A&A, 612, L6

Posti L., Marasco A., Fraternali F., Famaey B., 2019, A&A, 629, A59

Renzini A., 2020, MNRAS, 495, L42

Roberts M. S., 1962, AJ, 67, 437

Rodríguez-Puebla A., Behroozi P., Primack J., Klypin A., Lee C., Hellinger D., 2016, MNRAS, 462, 893

Romanowsky A. J., Fall S. M., 2012, ApJS, 203, 17

Romeo A. B., 2020, MNRAS, 491, 4843

Sánchez S. F. et al., 2012, A&A, 538, A8

Serra P. et al., 2012, MNRAS, 422, 1835

Sharma S., Steinmetz M., Bland-Hawthorn J., 2012, ApJ, 750, 107

Sorce J. G., Tully R. B., Courtois H. M., Jarrett T. H., Neill J. D., Shaya E. J., 2014, MNRAS, 444, 527

Stewart K. R. et al., 2017, ApJ, 843, 47

Stott J. P. et al., 2016, MNRAS, 457, 1888

Toomre A., 1964, ApJ, 139, 1217

van Dokkum P. G., Abraham R., Merritt A., Zhang J., Geha M., Conroy C., 2015, ApJL, 798, L45

Verheijen M. A. W., 2001, ApJ, 563, 694

Verheijen M. A. W., Sancisi R., 2001, A&A, 370, 765

Walter F., Brinks E., de Blok W. J. G., Bigiel F., Kennicutt Robert C. J., Thornley M. D., Leroy A., 2008, AJ, 136, 2563

Wang J., Koribalski B. S., Serra P., van der Hulst T., Roychowdhury S., Kamphuis P., Chengalur J. N., 2016, MNRAS, 460, 2143

Zasov A. V., 1974, Astron. Zh., 51, 1225

Zasov A. V., Zaitseva N. A., 2017, Astron. Lett., 43, 439

Zjupa J., Springel V., 2017, MNRAS, 466, 1625

Zolotov A. et al., 2015, MNRAS, 450, 2327

APPENDIX A: DATA

In this appendix, we present the data and the kinematic analysis of 2 H I-bearing ultra-diffuse galaxies (HUDs) and eight early-type galaxies. In Figs A1–A10, we show (i) the integrated H I intensity map contours overlaid on the optical image, (ii) Position-velocity diagram taken along the major axis of the galaxy with the rotation curves overlaid on them. The dashed lines indicate the systemic velocity and kinematic centre. The overplotted violet triangles represent the rotation curve derived by 'FAT', (iii) the intensity-weighted first moment of the galaxy, and (iv) velocity field of the best-fitting FAT model for all the HUDs and early-type galaxies.
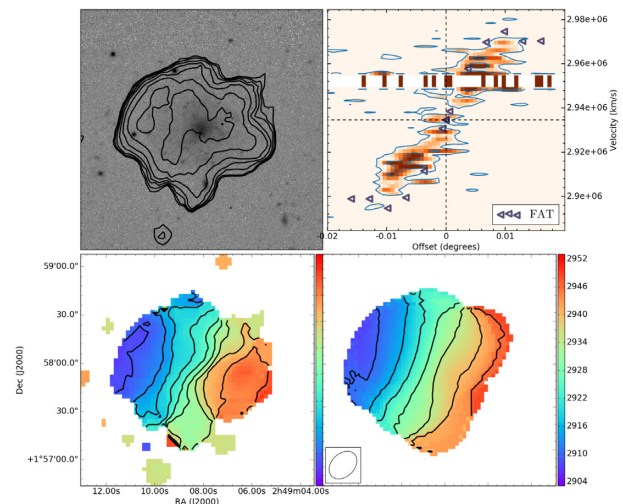

Figure A1. H I data and kinematics for the galaxy AGC121790. Top left: H I distribution of the galaxy overlaid on the SDSS *g*-band data. Top right: Position-velocity diagram (outer contour corresponds to 2σ) with the rotation curves overlaid on them. Bottom left: velocity field of data. and Bottom right: velocity field of the best-fitting FAT model. Velocity contours run from 2910 to 2946 km s^{-1} with a spacing of 6 km s^{-1}.
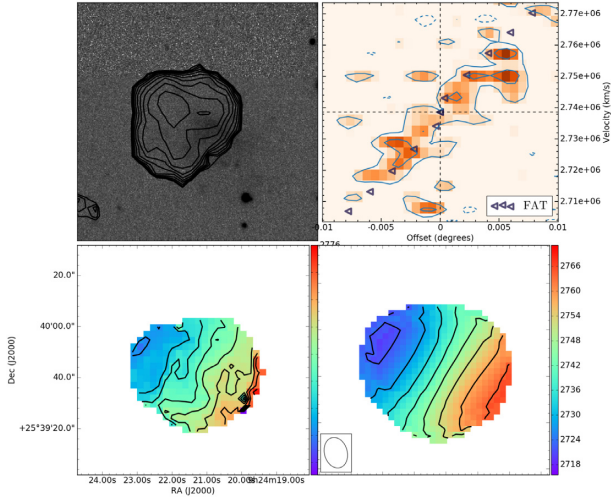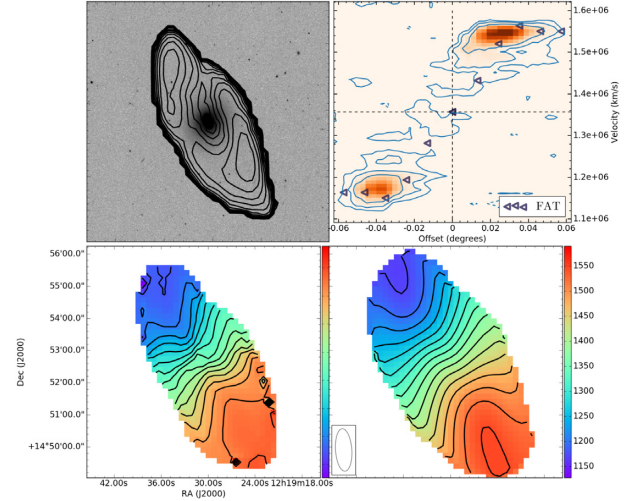
Figure A2. H I data and kinematics for the galaxy AGC749401. Top left: H I distribution of the galaxy overlaid on the SDSS *g*-band data. Top right: Position-velocity diagram (outer contour corresponds to 2σ) with the rotation curves overlaid on them. Bottom left: velocity field of data. Bottom right: velocity field of the best-fitting FAT model. Velocity contours run from 2712 to 2754 km s^{-1} with a spacing of 6 km s^{-1}.
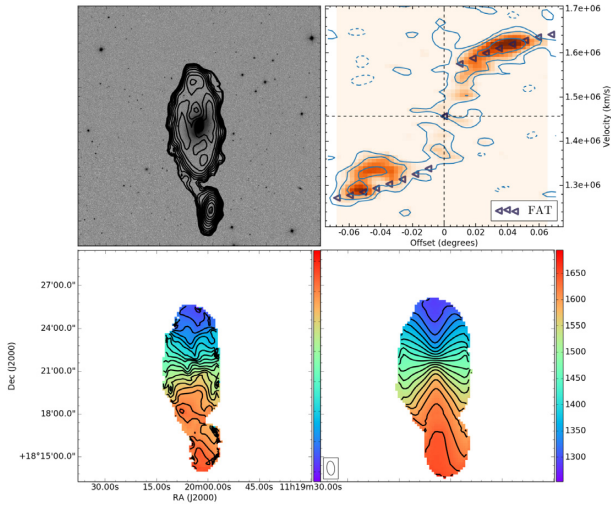

Figure A4. H I data and kinematics for the galaxy NGC 4262. Top left: H I distribution of the galaxy overlaid on the SDSS *g*-band data. Top right: Position-velocity diagram (outer contour corresponds to 2σ) with the rotation curves overlaid on them. Bottom left: velocity field of data. Bottom right: velocity field of the best-fitting FAT model. Velocity contours run from 1145 to 1545 km s^{-1} with a spacing of 25 km s^{-1}.

Figure A3. H I data and kinematics for the galaxy NGC 3626. Top left: H I distribution of the galaxy overlaid on the SDSS *g*-band data. Top right: Position-velocity diagram (outer contour corresponds to 2σ) with the rotation curves overlaid on them. Bottom left: velocity field of data. and Bottom right: velocity field of the best-fitting FAT model. Velocity contours run from 1300 to 1660 km s^{-1} with a spacing of 20 km s^{-1}.
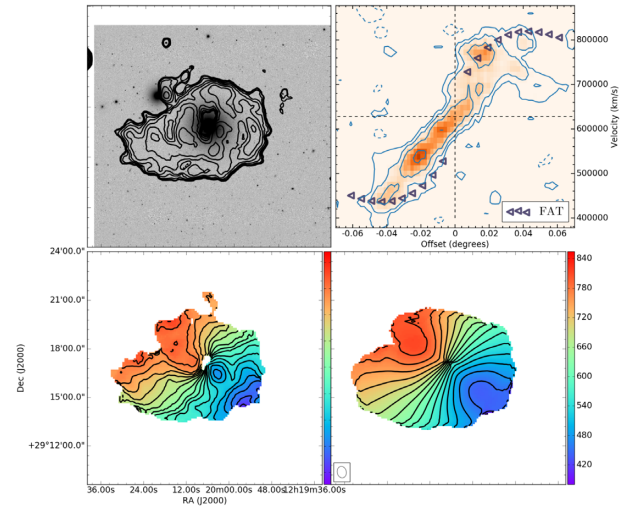

Figure A5. H I data and kinematics for the galaxy NGC 4278. Top left: H I distribution of the galaxy overlaid on the SDSS *g*-band data. Top right: Position-velocity diagram (outer contour corresponds to 2σ) with the rotation curves overlaid on them. Bottom left: velocity field of data. Bottom right: velocity field of the best-fitting FAT model. Velocity contours run from 425 to 800 km s^{-1} with a spacing of 25 km s^{-1}.
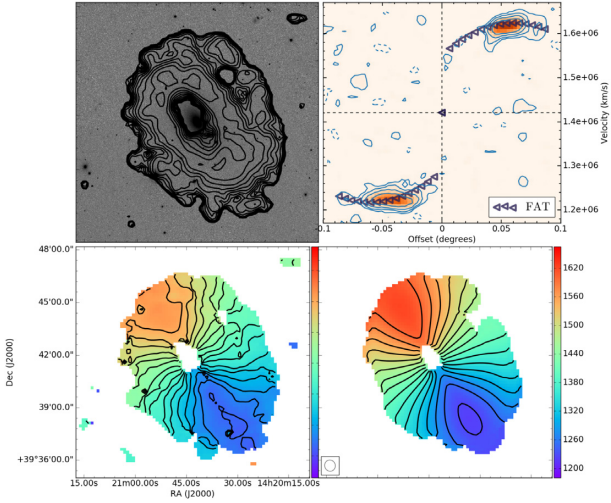
Figure A6. H I data and kinematics for the galaxy NGC 5582. Top left: H I distribution of the galaxy overlaid on the SDSS *g*-band data. Top right: Position-velocity diagram (outer contour corresponds to 2σ) with the rotation curves overlaid on them. Bottom left: velocity field of data. Bottom right: velocity field of the best-fitting FAT model. Velocity contours run from 1225 to 1600 km s^{-1} with a spacing of 25 km s^{-1}.
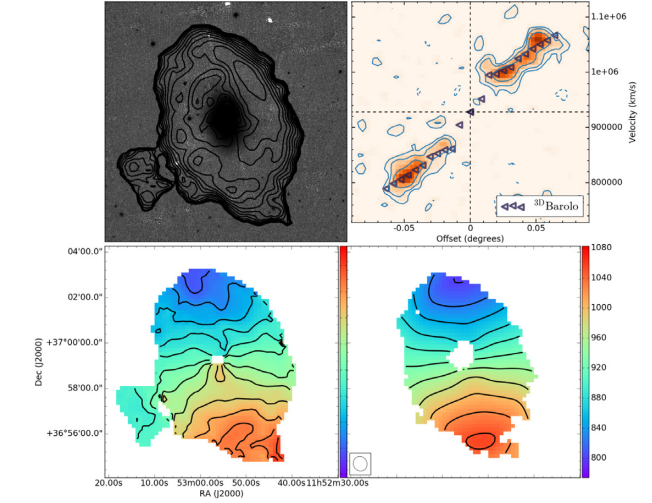

Figure A8. H I data and kinematics for the galaxy NGC 3941. Top left: H I distribution of the galaxy overlaid on the SDSS *g*-band data. Top right: Position-velocity diagram (outer contour corresponds to 2σ) with the rotation curves overlaid on them. Bottom left: velocity field of data. Bottom right: velocity field of the best-fitting FAT model. Velocity contours run from 800 to 1050 km s^{-1} with a spacing of 25 km s^{-1}.
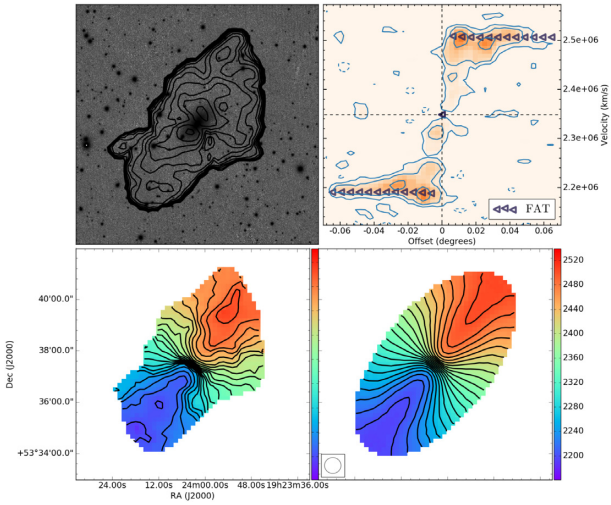

Figure A7. H I data and kinematics for the galaxy NGC 6798. Top left: H I distribution of the galaxy overlaid on the SDSS *g*-band data. Top right: Position-velocity diagram (outer contour corresponds to 2σ) with the rotation curves overlaid on them. Bottom left: velocity field of data. Bottom right: velocity field of the best-fitting FAT model. Velocity contours run from 2200 to 2500 km s^{-1} with a spacing of 15 km s^{-1}.
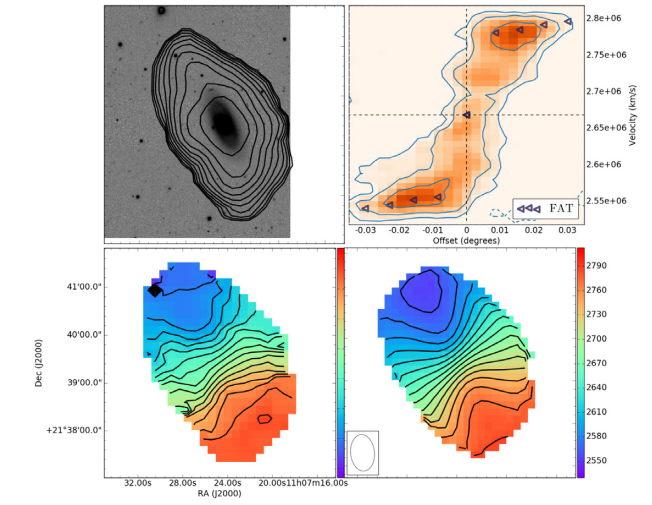

Figure A9. H I data and kinematics for the galaxy UGC6176. Top left: H I distribution of the galaxy overlaid on the SDSS *g*-band data. Top right: Position-velocity diagram (outer contour corresponds to 2σ) with the rotation curves overlaid on them. Bottom left: velocity field of data. Bottom right: velocity field of the best-fitting FAT model. Velocity contours run from 2560 to 2800 km s^{-1} with a spacing of 15 km s^{-1}.
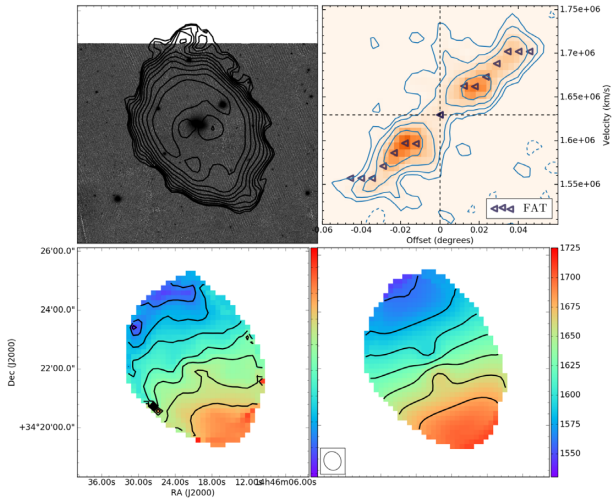
Figure A10. H I data and kinematics for the galaxy UGC9519. Top left: H I distribution of the galaxy overlaid on the SDSS *g*-band data. Top right: Position-velocity diagram (outer contour corresponds to 2σ) with the rotation curves overlaid on them. Bottom left: velocity field of data. Bottom right: velocity field of the best-fitting FAT model. Velocity contours run from 1560 to 1680 km s^{-1} with a spacing of 20 km s^{-1}.
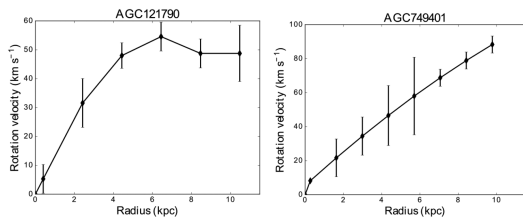

Figure A12. Rotation curves of early-type galaxies. Error bars on NGC 4278 are taken to be the velocity resolution of the data cube (13 km s^{-1}, which is greater than median of FAT errors of all galaxies) since FAT error bars were unreliable.

Figure A11. Rotation curves of ultra-diffuse galaxies, AGC121790 and AGC749401.
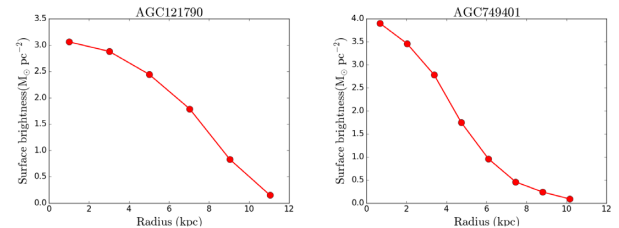
Figure A13. H I surface brightness as a function of radius for the ultra-diffuse galaxies AGC121790 and AGC749401, respectively.

Figure A14. H I surface brightness as a function of radius for the early-type galaxies NGC 3626, NGC 4262, NGC 4278, NGC 5582, NGC 6798, NGC 3941, UGC6176, and UGC9519, respectively.
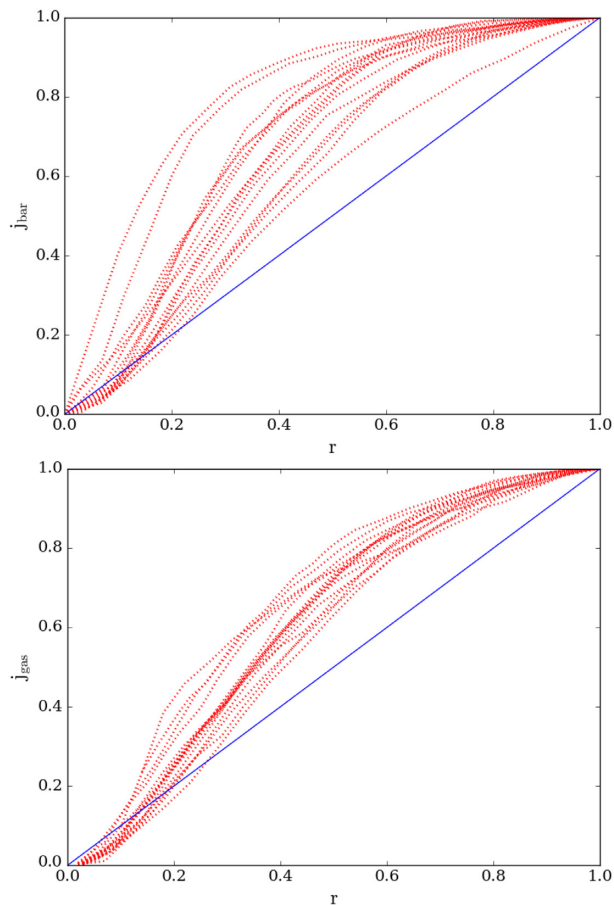
Figure A15. The cumulative j_{bar} and j_g profiles of 16 UMa spirals. We normalize the axes to allow the comparison between the profiles. The one-to-one relation is shown with a blue solid line.

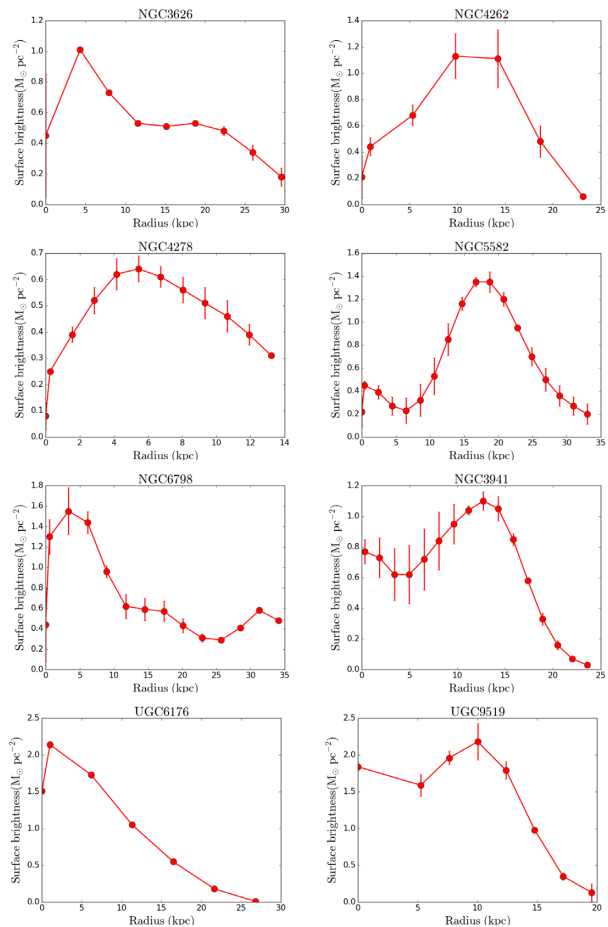**Figure A17.** The cumulative j_g profiles of eight early-type galaxies. We normalize the axes to allow the comparison between the profiles. The one-to-one relation is shown with a blue solid line.
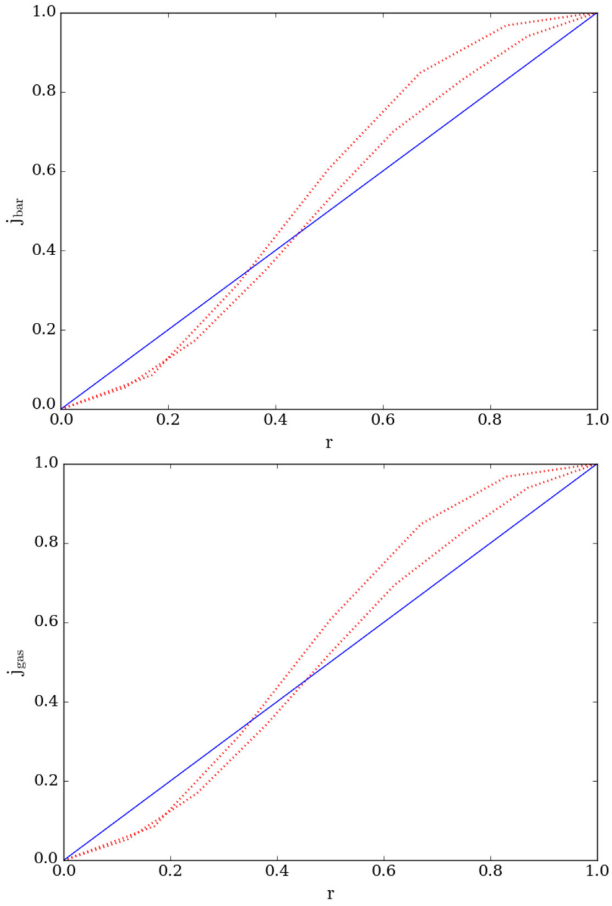
Figure A16. The cumulative j_{bar} and j_g profiles of two ultra-diffuse galaxies. We normalize the axes to allow the comparison between the profiles. The one-to-one relation is shown with a blue solid line.
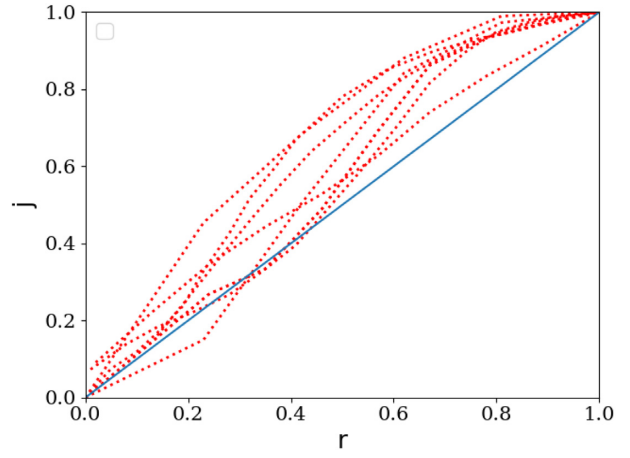
Table A1. Measured values of specific angular momentum and mass (stars, gas, and baryons) for ultra-diffuse galaxies in this study.

Galaxy	Dist (Mpc)	M_s (log$_{10}$ M$_\odot$)	M_g (log$_{10}$ M$_\odot$)	M_{bar} (log$_{10}$ M$_\odot$)	j_s (log$_{10}$ kpc km/s)	j_g (log$_{10}$ kpc km/s)	j_{bar} (log$_{10}$ kpc km/s)
AGC749401	41.8	7.31 ± 0.131	8.66 ± 0.137	8.68 ± 0.131	2.12 ± 0.110	2.39 ± 0.093	2.39 ± 0.092
AGC121790	37.5	6.40 ± 0.131	8.89 ± 0.137	8.89 ± 0.136	2.00 ± 0.081	2.46 ± 0.074	2.46 ± 0.075

Table A2. Measured values of specific angular momentum and mass (stars, gas, and baryons) for UMa spiral galaxies in this study.

Galaxy	Dist (Mpc)	M_s (log$_{10}$ M$_\odot$)	M_g (log$_{10}$ M$_\odot$)	M_{bar} (log$_{10}$ M$_\odot$)	j_s (log$_{10}$ kpc km/s)	j_g (log$_{10}$ kpc km/s)	j_{bar} (log$_{10}$ kpc km/s)
NGC 3877	15.27	10.6 ± 0.170	9.14 ± 0.137	10.62 ± 0.164	2.87 ± 0.065	3.04 ± 0.142	2.88 ± 0.066
NGC 3917	17.14	10.13 ± 0.170	9.34 ± 0.137	10.19 ± 0.147	2.75 ± 0.065	3.07 ± 0.169	2.81 ± 0.077
NGC 3953	18.82	10.73 ± 0.170	9.62 ± 0.137	10.76 ± 0.158	3.14 ± 0.067	3.46 ± 0.120	3.17 ± 0.068
NGC 3972	20.04	10.10 ± 0.170	9.31 ± 0.137	10.16 ± 0.147	2.70 ± 0.066	2.98 ± 0.132	2.75 ± 0.071
NGC 3992	27.04	10.91 ± 0.170	10.23 ± 0.137	11.0 ± 0.143	3.36 ± 0.068	3.84 ± 0.068	3.49 ± 0.068
NGC 4013	19.23	10.81 ± 0.170	9.65 ± 0.137	10.84 ± 0.159	2.93 ± 0.065	3.42 ± 0.065	2.99 ± 0.065
NGC 4100	20.04	10.62 ± 0.170	9.74 ± 0.137	10.67 ± 0.151	3.01 ± 0.066	3.39 ± 0.156	3.07 ± 0.074
NGC 4157	16.29	10.87 ± 0.170	9.96 ± 0.137	10.92 ± 0.152	2.92 ± 0.065	3.40 ± 0.097	3.01 ± 0.068
NGC 4183	17.21	10.12 ± 0.170	9.65 ± 0.137	10.25 ± 0.132	2.76 ± 0.066	3.06 ± 0.137	2.85 ± 0.082
NGC 4217	18.19	10.75 ± 0.170	9.53 ± 0.137	10.78 ± 0.161	2.97 ± 0.065	3.27 ± 0.114	2.99 ± 0.066
UGC6399	22.08	9.48 ± 0.171	9.19 ± 0.137	9.66 ± 0.122	2.54 ± 0.069	2.79 ± 0.141	2.64 ± 0.091
UGC6446	18.03	8.83 ± 0.172	9.62 ± 0.137	9.69 ± 0.121	2.29 ± 0.088	2.88 ± 0.100	2.83 ± 0.112
UGC6667	18.45	9.80 ± 0.170	9.06 ± 0.137	9.87 ± 0.145	2.67 ± 0.065	2.70 ± 0.125	2.67 ± 0.068
UGC6917	20.41	9.42 ± 0.171	9.54 ± 0.137	9.78 ± 0.107	2.67 ± 0.073	2.99 ± 0.117	2.88 ± 0.101
UGC6983	21.28	9.29 ± 0.170	9.74 ± 0.137	9.87 ± 0.111	2.62 ± 0.071	3.08 ± 0.095	3.00 ± 0.091
UGC7089	11.50	9.06 ± 0.171	8.80 ± 0.137	9.25 ± 0.120	2.19 ± 0.067	2.54 ± 0.066	2.34 ± 0.067

Table A3. Measured values of gas mass and gas specific angular momentum of six S0 and two elliptical galaxies in this study.

Galaxy	Morp	Dist (Mpc)	M_g (log$_{10}$ M$_\odot$)	j_g (log$_{10}$ kpc km s^{-1})	Notes
NGC 3626	S0	19.5	9.19 ± 0.137	3.60 ± 0.073	C
NGC 4262	S0	15.4	8.84 ± 0.137	3.27 ± 0.086	R
NGC 4278	E	15.6	8.90 ± 0.137	3.64 ± 0.091	M, L
NGC 5582	E	27.7	9.78 ± 0.137	3.85 ± 0.074	R
NGC 3941	S0	11.9	8.86 ± 0.137	3.15 ± 0.073	C, R
NGC 6798	S0	37.5	9.64 ± 0.137	3.67 ± 0.077	C
UGC6176	S0	40.1	9.21 ± 0.137	3.21 ± 0.068	W
UGC9519	S0	27.6	9.40 ± 0.137	3.02 ± 0.081	M

Note. Notes on H I morphology and kinematics: C = H I counter-rotating relative to the stellar kinematics;
L = lopsided H I morphology; M = H I misaligned relative to the stellar kinematics; R = ring; W = warp.

Table A4. Convergence factors of 16 UMa spirals for j_{bar} and j_g profiles.

Galaxy	r_{bar}	r_g
N3877	0.90	0.90
N3917	0.94	0.86
N3953	0.98	0.90
N3972	0.94	0.82
N3992	0.97	0.95
N4013	0.97	0.88
N4100	0.96	0.90
N4157	0.95	0.88
N4183	0.91	0.82
N4217	0.97	0.83
U6399	0.86	0.78
U6446	0.94	0.94

Table A4 *– continued*

Galaxy	r_{bar}	r_g
U6667	0.66	0.73
U6917	0.89	0.88
U6983	0.94	0.94
U7089	0.82	0.86

Table A5. Convergence factors of two ultra-diffuse galaxies for j_{bar} and j_g profiles.

Galaxy	r_{bar}	r_g
AGC121790	0.74	0.74
AGC749401	0.61	0.60

Table A6. Convergence factors of eight early-type galaxies for j_g profiles.

Galaxy	r_g
NGC 4262	0.80
NGC 4278	0.71
NGC 3626	0.61
NGC 3941	0.89
NGC 5582	0.85
NGC 6798	0.43
UGC9519	0.74
UGC6176	0.85

This paper has been typeset from a TEX/LATEX file prepared by the author.